25th ABCM International Congress of Mechanical Engineering
October 20-25, 2019, Uberlândia, MG, Brazil

COB-2019-0132
NUMERICAL EVALUATION OF LOW VELOCITY IMPACT DAMAGE ON COMPOSITE PLATES SUBJECTED TO COMPRESSIVE PRELOAD

Felipe Ruivo Fuga
Maurício Vicente Donadon
ITA, Technological Institute of Aeronautics, Department of Aeronautics, São José dos Campos, Brazil
fuga@ita.br (Felipe Ruivo Fuga), donadon@ita.br (Maurício Vicente Donadon)

Abstract. *A finite element model for low velocity impact damage of composite laminated plates subjected to compressive preload is presented using ABAQUS FE code. Intralaminar damage is evaluated in each ply using a progressive failure model based on Continuum Damage Mechanics approach for fibre-reinforced composites while the interlaminar damage is evaluated using cohesive elements placed at the laminate's mid plane. Impact simulations were carried out at different preload stress levels, ranging from unloaded until a post-buckled regime. The total cohesive zone damaged area and total dissipated energy during impact was correlated to the incident impact energy and preload stress level.*

Keywords: *Composite damage, Low velocity impact, Finite element analysis (FEA)*

1. INTRODUCTION

Fibre-reinforced composite materials have been a subject of interest for the aerospace industries due to their high weight-specific mechanical properties. As the aircraft industry demands lower operational and maintenance costs, longer inspection intervals and damage tolerant structures became design requirements.

During manufacture, service and maintenance operations, foreign object impacts represent a potential structural integrity threat, since the extension of induced damage in composites is often not detectable by visual inspection. Moreover, composite laminates are susceptible to strength reduction due to intralaminar and interlaminar damage. Despite the impact dynamics of composite laminates have been extensively studied in the literature, as presented in a unified comprehensive manner by Abrate (1998), most of the work has focused on unloaded laminates.

Davies and Zhang (1995) suggested that the onset of delamination in composite laminated plates during impact is determined by a force threshold, known as delamination threshsold load (DTL), which can be analytically estimated as function of critical energy release rate G_{IIc} for mode two delamination. Olsson (2003) presented a closed form solution for the DTL with the assumptions of Hertzian contact law for monolithic composite plates. The effects of in plane compressive pre-load followed by impact on composite laminates were studied by Zhang *et al.* (1999), where three characteristic non-dimensional parameters were suggested in order to assess the nature of impact damage.

Finite element implementations of the impact damage dynamics with compressive pre-load have been described in the literature. Zhang *et al.* (1999) divided the preload followed by impact event in two steps. For the first a dynamic relaxation technique was used in order to predict the buckling shape. Then an explicit dynamic simulation was carried out for the impact event. Heimbs *et al.* (2009) performed all calculations during the same step, but only for pre-loads below buckling.

The current paper aims to show the implementation of a finite element model, using ABAQUS FE code, capable to predict intralaminar such as interlaminar damage in composite laminates subjected to compressive preload below and above axial compressive buckling load.

2. INTRALAMINAR DAMAGE

Damage initiation and evolution within the laminate plies are modelled by the methodology presented by Yokoyama *et al.* (2010). This damage model combines a stress based approach for damage initiation with continuum damage mechanics (CDM) as well as fracture mechanics using a smeared cracking formulation. The implementation of the algorithm in ABAQUS/EXPLICIT is performed via user defined material (VUMAT) for shell elements.

Hashin (1980) presented a failure criteria for unidirectional fibre composite materials which account for the prediction of four different failure modes. Two of them relative to the fibre direction (direction 1 in lamina coordinate system) and the other two relative to the matrix (direction 2 in lamina coordinate system). In this assumption, failure is predicted by the evaluation of a stress state where normal and in-plane shear stresses are coupled together. For composite materials

with woven fabrics, directions 1 and 2, in the lamina coordinate system, have fibres as reinforcement. Therefore, in order to predict damage initiation for woven fabrics, the maximum stress criteria are used, given as follows.

Tensile failure mode (direction 1):

$$\frac{\sigma_{11}}{X_t} \geq 1; \tag{1}$$

Compression failure mode (direction 1):

$$\frac{|\sigma_{11}|}{X_c} \geq 1; \tag{2}$$

Tensile failure mode (direction 2):

$$\frac{\sigma_{22}}{Y_t} \geq 1; \tag{3}$$

Compression failure mode (direction 2):

$$\frac{|\sigma_{22}|}{Y_c} \geq 1; \tag{4}$$

In-plane shear failure mode:

$$\frac{|\tau_{12}|}{S_{12}} \geq 1; \tag{5}$$

Once the failure criteria for direction 1 are met, damage evolution is predicted based on the following expression,

$$d_{11} = \lambda_1^I + \lambda_2^I - \lambda_1^I \lambda_2^I \tag{6}$$

where

$$\lambda_1^I = \left(\frac{2G_1^t}{2G_1^t - X_t l^* \epsilon_{1,0}^t} \right) \left(\frac{\epsilon_1^t - \epsilon_{1,0}^t}{\epsilon_1^t} \right) \tag{7}$$

and

$$\lambda_2^I = \left(\frac{2G_1^c}{2G_1^c - X_c l^* \epsilon_{1,0}^c} \right) \left(\frac{\epsilon_1^c - \epsilon_{1,0}^c}{\epsilon_1^c} \right) \tag{8}$$

G_1^t and G_1^c represent the intralaminar fracture toughness for the direction 1 in tension and compression, respectively. Likewise, X_t and X_c denote the strength for direction 1 in tension and compression. Finally, damage initiation strains are represented by $\epsilon_{1,0}^t$ and $\epsilon_{1,0}^c$. ϵ_1 is the strain in direction 1 at the current timestep, which can be tensile or compressive.

Likewise for direction 2:

$$d_{22} = \lambda_1^{II} + \lambda_2^{II} - \lambda_1^{II} \lambda_2^{II} \tag{9}$$

where

$$\lambda_1^{II} = \left(\frac{2G_2^t}{2G_2^t - Y_t l^* \epsilon_{2,0}^t} \right) \left(\frac{\epsilon_2^t - \epsilon_{2,0}^t}{\epsilon_2^t} \right) \tag{10}$$

and

$$\lambda_2^{II} = \left(\frac{2G_2^c}{2G_2^c - Y_c l^* \epsilon_{2,0}^c} \right) \left(\frac{\epsilon_2^c - \epsilon_{2,0}^c}{\epsilon_2^c} \right). \tag{11}$$

In a similar way, the variables G_2^t, G_2^c, Y_t, Y_c, $\epsilon_{2,0}^t$, $\epsilon_{2,0}^c$ and ϵ_2 represent the same material properties as before, but now for direction 2 in the lamina coordinate system.

The in-plane shear stress-strain behaviour, Eq. 12, is defined as non-linear elasto-plastic relation

$$\tau_{12} = G_{12} \gamma_{12} \tag{12}$$

where G_{12} is a function of the current shear strain, given as

$$G_{12} = G_{12}^0 + c_1 \left(e^{-c_2\gamma_{12}} - 1\right). \tag{13}$$

The inelastic shear strain γ_{12}^{in} is obtained by the difference between the total and elastic strains

$$\gamma_{12}^{in} = \gamma_{12} - \frac{\tau_{12}}{G_{12}^0} \tag{14}$$

therefore, the total damage due to shear loading is defined as:

$$d_{12} = \frac{\gamma_{12}^{ult} 2 \left(\gamma_{12} - \gamma_{12}^{in,0}\right) - \gamma_{12}^{ult}}{\left(\gamma_{12}^{ult} + \gamma_{12}^{in,0} - \gamma_{12}\right)\left(\gamma_{12} - \gamma_{12}^{in,0}\right)} \tag{15}$$

where $\gamma_{12}^{in,0}$ and γ_{12}^{ult} represent the inelastic shear strain at damage initiation and ultimate strain before complete failure, respectively. The ultimate strain is determined as a function of the in plane shear intralaminar fracture toughness G_S as follows:

$$\gamma_{12}^{ult} = \frac{2G_S}{S_{12}l^*} \tag{16}$$

With all damage variables defined, at a given time-step, the degraded stress state can be defined.

$$\begin{Bmatrix}\sigma_{11}\\ \sigma_{22}\\ \sigma_{12}\end{Bmatrix}^d = \begin{bmatrix}1-d_{11} & 0 & 0\\ 0 & (1-d_{11})(1-d_{22}) & 0\\ 0 & 0 & 1-d_{12}\end{bmatrix} \begin{Bmatrix}\sigma_{11}\\ \sigma_{22}\\ \sigma_{12}\end{Bmatrix}^e \tag{17}$$

3. INTERLAMINAR DAMAGE

Interlaminar damage initiation and propagation is evaluated by the use of decohesion elements at the laminate's mid-plane interface. The element formulation is based on the work of Camanho *et al.* (2003), which has the capability of predicting the onset of the softening process by a strength failure criteria and delamination propagation by the use of Fracture Mechanics.

The cohesive region constitutive relation in the undamaged regime is described by the use of a penalty stiffness E_{ii} and the elastic stresses associated with each delamination mode (I, II and III) are given by,

$$\begin{Bmatrix}\sigma_I\\ \sigma_{II}\\ \sigma_{III}\end{Bmatrix} = \begin{bmatrix}E_{nn} & 0 & 0\\ 0 & E_{ss} & 0\\ 0 & 0 & E_{tt}\end{bmatrix} \begin{Bmatrix}\epsilon_n\\ \epsilon_s\\ \epsilon_t\end{Bmatrix}. \tag{18}$$

Strains are determined in therms of the effective displacements, as shown:

$$\begin{Bmatrix}\epsilon_n & \epsilon_s & \epsilon_t\end{Bmatrix}^T = \begin{Bmatrix}\frac{\delta_n}{T_0} & \frac{\delta_s}{T_0} & \frac{\delta_t}{T_0}\end{Bmatrix}^T \tag{19}$$

where T_0 is the cohesive element's thickness. Damage onset is determined by the maximum stress criteria:

$$max\left(\frac{\sigma_I}{\sigma_I^0}, \frac{\sigma_{II}}{\sigma_{II}^0}, \frac{\sigma_{III}}{\sigma_{III}^0}\right) = 1, \tag{20}$$

where σ_I^0,σ_{II}^0 and σ_{III}^0 are the limit stresses for each delamination mode. Effective displacement is calculated as follows:

$$\delta_m = \sqrt{\delta_n^2 + \delta_s^2 + \delta_t^2} \tag{21}$$

Once the strength failure criteria is satisfied, softening is performed by the use of a linear softening law, Fig. 1, where D is the damage scalar variable and $\overline{\sigma}_i$ are the stress components predicted by the undamaged constitutive relation.

$$\begin{Bmatrix}\sigma_I\\ \sigma_{II}\\ \sigma_{III}\end{Bmatrix} = \begin{bmatrix}(1-D) & 0 & 0\\ 0 & (1-D) & 0\\ 0 & 0 & (1-D)\end{bmatrix} \begin{Bmatrix}\overline{\sigma}_I\\ \overline{\sigma}_{II}\\ \overline{\sigma}_{III}\end{Bmatrix} \tag{22}$$

$$D = \frac{\delta^{ult}\left(\delta_m - \delta^0\right)}{\delta_m\left(\delta^{ult} - \delta^0\right)} \tag{23}$$

In order to evaluate the energy release rate at each fracture direction, the mixed mode fractions are calculated as follows:

$$\phi_I = \frac{G_I}{G_I + G_{II} + G_{III}} \tag{24}$$

$$\phi_{II} = \frac{G_{II}}{G_I + G_{II} + G_{III}} \tag{25}$$

$$\phi_{III} = 1 - (\phi_2 + \phi_1) \tag{26}$$

where G_I, G_{II} and G_{III} represent the work done by each traction mode

$$G_i = \int_0^{\delta_i} \sigma_i d\delta_i. \tag{27}$$

The mixed mode delamination fracture toughness is determined by Eq. 28, derived from the power law criterion. The displacement at failure and damage variables are defined in terms of the fracture toughness G_c, which correspond to the area underneath the stress-relative displacement curve depicted in Fig. 1.

$$G_c = \left[\frac{1}{\left(\frac{\phi_I}{G_{Ic}}\right)^{\alpha} + \left(\frac{\phi_{II}}{G_{IIc}}\right)^{\alpha} + \left(\frac{\phi_{III}}{G_{IIIc}}\right)^{\alpha}} \right]^{\frac{1}{\alpha}} \tag{28}$$

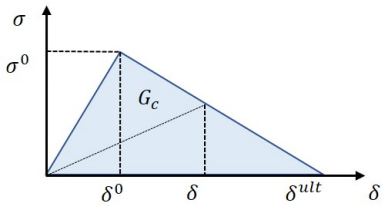

Figure 1. Equivalent traction separation relation.

4. FINITE ELEMENT MODEL

The composite laminate consists of 8 plys of 0.25 mm thickness each, stacking sequence $[(0/\pm 45/90)_2]$ and dimensions 150 mm x 100 mm. Four noded shell elements with reduced integration (S4R) were used to model the laminate. Material constitutive relation, is defined via user material model (VUMAT). Transverse shear effects are determined by the laminate constants K_{11} and K_{22}, which can be found as a result of a data check analysis for a conventional orthotropic material in ABAQUS FE code material library. The mechanical properties at ply level are listed in Tables 1 and 2.

Table 1. Lamina properties.

E_1 (GPa)	E_2(GPa)	ν_{12}	G^0_{12}(GPa)	c_1(GPa)	c_2	K_{11}	K_{22}	ρ (Ton/mm^3)
51.83	51.83	0.064	2.82	25	26	836.32	836.32	$1.6\ 10^{-9}$

Table 2. Lamina strength and fracture properties.

X_t (MPa)	X_c (MPa)	Y_t(MPa)	Y_c(MPa)	S(MPa)
665	435	665	435	94.5
G^t_1(kJ/m^2)	G^c_1(kJ/m^2)	G^t_2(kJ/m^2)	G^c_2(kJ/m^2)	G_S(kJ/m^2)
77	4.3	77	4.3	2

A single layer of COH3D8 interface elements available in ABAQUS was introduced at the midplane of the stack. 10% of a ply thickness is assumed for the cohesive interface thickness. Displacement compatibility is obtained by the use of a surface to surface *TIE* constraint. Mechanical properties of cohesive elements are displayed in Tab. 3 and can be found at (Yokoyama, 2012). Regular mesh was used for both upper and lower sublaminates as well as the cohesive brick element,

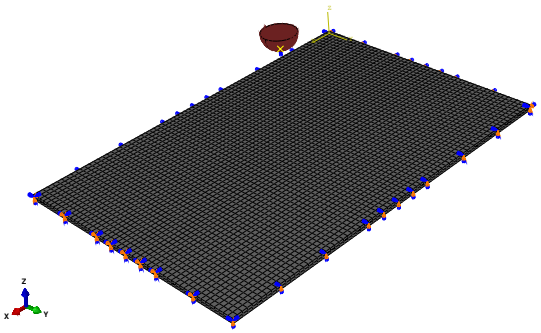

Figure 2. Finite element model.

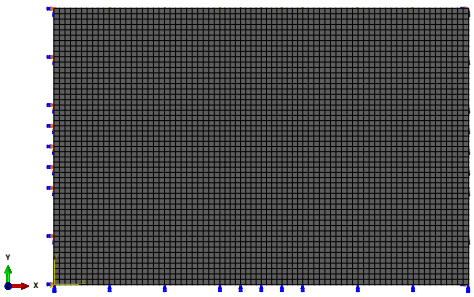

Figure 3. Regular mesh for shell and decohesive elements.

Fig.3. Impactor geometry is assumed hemispherical, modelled by an analytic rigid surface weighing 1.5 kg. The complete model is shown in Figure 2.

In order to impose the same amount of curvature in the laminate during post-buckling regime, the analysis is divided in two steps. Firstly, a linear buckling analysis is performed by the use of Lanczos solver algorithm, where only the first eigenvalue and eigenvector are stored. The following step is a dynamic analysis, based on the explicit time integration scheme, where the in plane loading and impact event occur. At this step, the displacement field of first buckling shape can be used to generate an initial mesh perturbation, providing the same stable equilibrium condition, before impact, for each pre-load beyond bifurcation point. Loaded edges are considered clamped while the unloaded are simply supported. Impactor has all DOF's fixed for the linear buckling analysis, while vertical displacement is allowed in step 2. Penalty contact based formulation is defined between impactor and the upper laminate face, disregarding friction effects. Figure 4 shows the relation between the two calculation steps employed in the model.

Table 3. Traction separation properties.

E_{nn} (MPa)	E_{ss} (MPa)	E_{tt} (MPa)	ρ (ton/mm^3)	G_{Ic} (kJ/m^2)
2970	1080	1080	$1.2\ 10^{-7}$	0.483
G_{IIc}(kJ/m^2)	G_{IIIc}(kJ/m^2)	σ_I^0 (MPa)	σ_{II}^0 (MPa)	σ_{III}^0(MPa)
4.298	4.298	50	21.2	21.2

Five levels of incident energy are chosen, ranging from 3 to 25.23 J. Five levels of pre-load are also specified, those being 0%, 30%, 60%, 105% and 120% of the first buckling load.

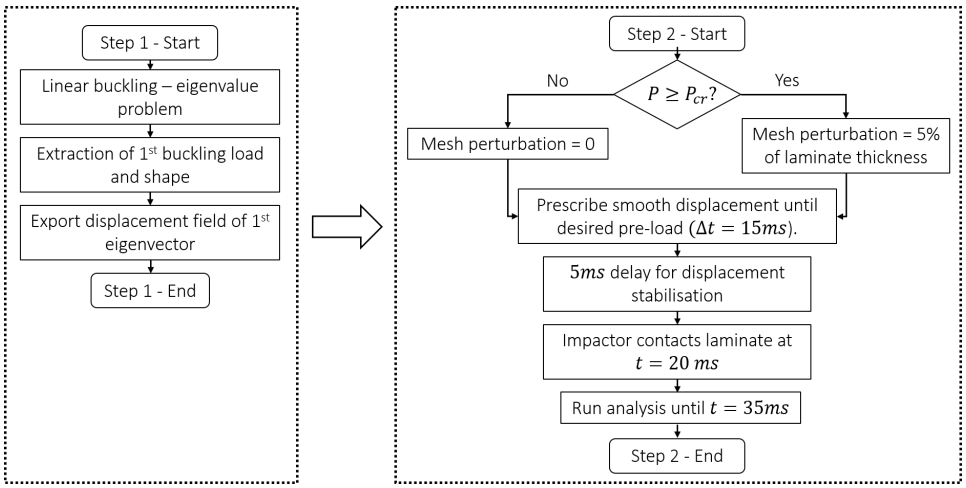

Figure 4. Finite element calculation steps.

During the analysis's dynamic step, time integration is performed explicitly. Consequently, mesh refinement plays an important role in stable time increment. As a result of the cohesive interface thickness being small, stable time increment is also small and analysis total time becomes very large. Therefore the density of cohesive elements was altered by 2 orders of magnitude, minimising analysis total elapsed time. Despite the laminate being more massive, altering dynamic oscillations in time history, the impact analysis is done in the low energy regime where dynamics effects are often negligible.

In order to compare impact force and displacement time history, a model without damage propagation is created. This model consists of the same rigid impactor and a purely elastic laminate modelled with four noded shell elements (S4R), constitutive relation described by the ABAQUS's in-built orthotropic material and no cohesive interface.

5. RESULTS

Figure 5 presents the first buckling shape obtained by the linear buckling analysis. A mesh with mean element size of 2 mm and 11856 elements was generated. The first buckling load is equal to 14.224 kN, which corresponds to an axial displacement of 0.292 mm. The reduction of mean element size from 2 mm to 1.5 mm resulted in much larger total elapsed time, and little difference in time histories and damaged area (S_d). Therefore the coarse mesh was used.

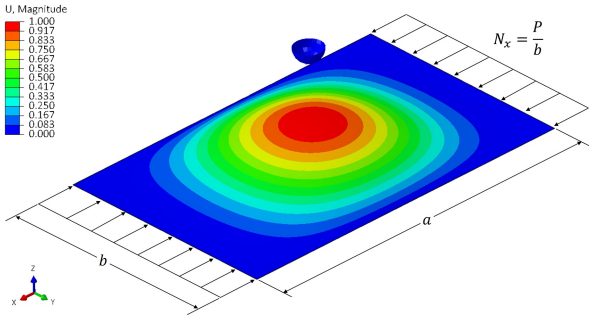

Figure 5. First buckling mode shape.

Vertical displacement histories, at the plate's center, of two energy levels and three load cases are presented in Fig 6, where is noticeable that for low energy levels the purely elastic and damage propagating models present similar response. However, for higher energy levels, damage propagation result in longer contact time and higher maximum displacement. The figure also shows the condition before impact for the cases loaded above buckling point.

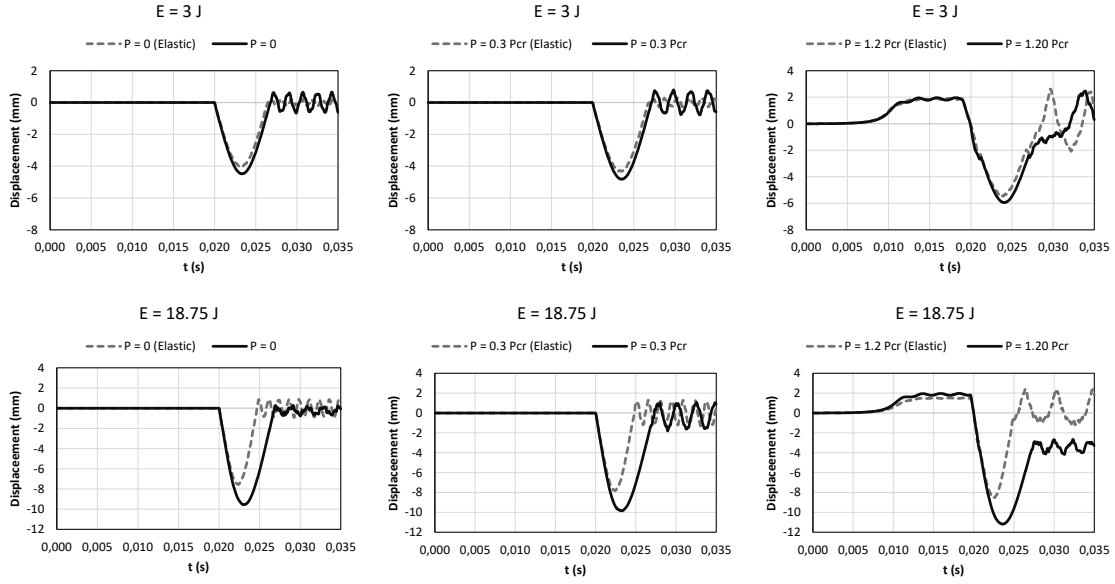

Figure 6. Displacement history comparison between FE predictions obtained using elastic and damage propagating models.

The impact load histories, Fig 7, also shows the same behaviour at low energy levels, but big difference for higher incident energy. At higher levels is clear that there is a maximum contact force level from which the material is unable to withstand further load.

Impact load versus displacement curves, Fig 8, show the influence of pre-load on the plate's bending stiffness. Maximum displacement is greater as pre-load increases. Load cases above buckling present a displacement of about 2 mm

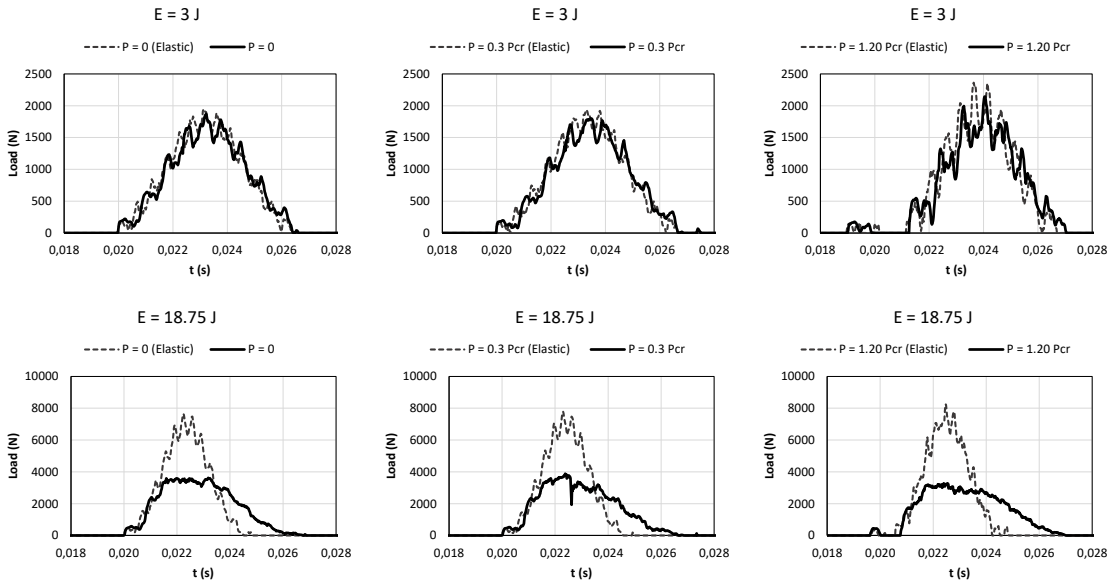

Figure 7. Force history comparison between FE predictions obtained using elastic and damage propagating models.

before impact, resulting in two impact events. Load-displacement curves also shows a comparison between the analytical DTL, calculated as presented by Olsson (2003), and the DTL indicated by the plateau level predicted using the proposed numerical model. Total energy dissipated during impact can be calculated by integrating the load-displacement curves, where the dissipated energy is equal to the area inside the looping defined by loading-unloading paths.

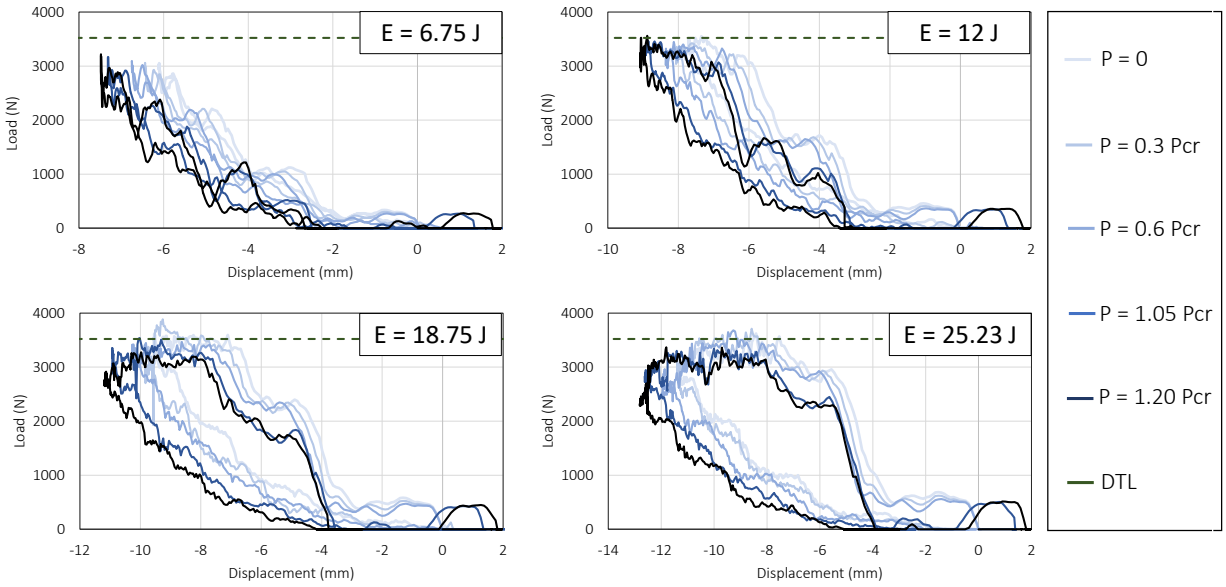

Figure 8. Effects of pre-load and impact energy on the overall plate stiffness for damage propagating models.

Total dissipated energy during impact is plotted as a percentage of incident energy and pre-load level, Fig 9. As the pre-load increases, energy dissipation becomes greater. At low energy levels the influence of pre-stress above buckling is grater. For higher incident energies the total dissipation of energy variation becomes smaller.

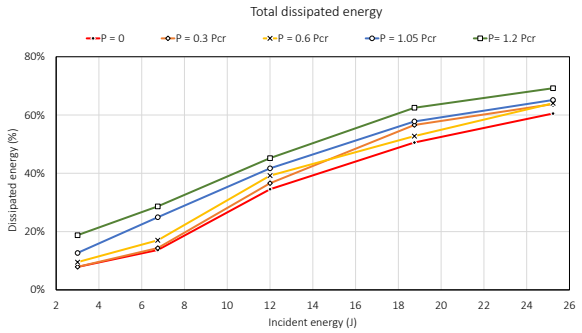

Figure 9. Relative dissipated energy versus incident energy.

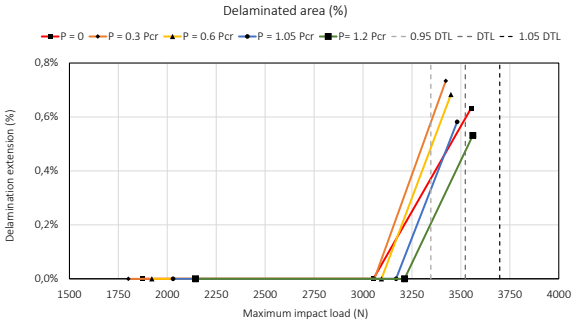

Figure 10. Delamination threshold load.

The cohesive interface damage parameter D is shown in Fig. 11 for all energy levels and three load cases. The interlaminar damage extension has a strong dependence on the incident energy. The cases loaded above buckling presented more interlaminar degradation near the edges of the laminate, since the post-buckling shape introduces curvatures in the plate. For higher energy levels, maximum displacement and curvature, induced by impact, are great enough that damage near the edges is observed for most of the pre-load levels.

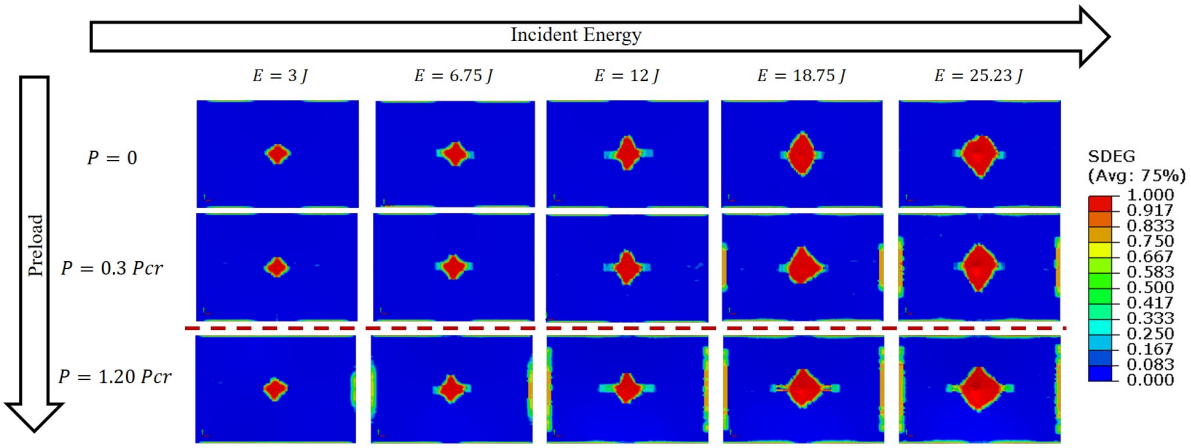

Figure 11. Cohesive degradation parameter (predicted mid-plane delaminated area).

Figure 10 shows the delamination extension as a function of the maximum contact load. Incident energies of 3 J and 6.75 J resulted in peak loads around 2 and 3 kN, respectively, and no delaminated region. 12 J of incident energy, resulted in a delamination area extension under 1%. Therefore, the maximum load predicted for this case is high enough to just start the delamination. The figure correlates the load at which delamination became noticeable with the theoretical value within a marign of $\pm$ 5% error.

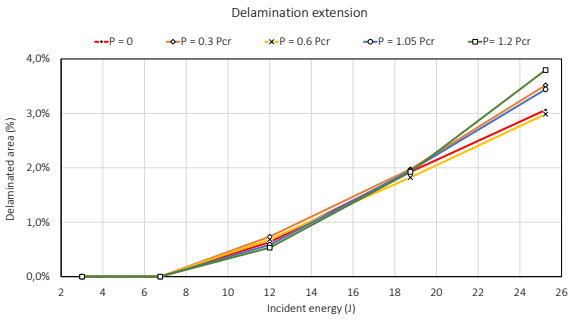

Figure 12. Total delaminated area.

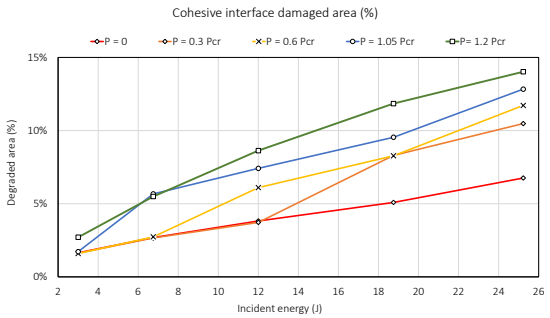

Figure 13. Cohesive interface damaged area.

The total delamination extension, calculated as the number of elements with degradation parameter $D = 1$, presented little dependence on the pre-load level, Fig. 12. For higher energy levels the variation between load cases becomes greater. However the total damaged cohesive area, obtained by the number of elements with $D > 0$ increases as the pre-stress

becomes greater, Fig. 13. The difference between load cases is a result of degraded elements near the clamped edges.

Intralaminar damage is displayed in Figures 14 and 15 for three energy and pre-load levels. Figure 14 shows the damage due to compression along direction 2 at the laminate's top ply, which contacts the impactor. The length of damaged elements is greater for pre-load levels beyond buckling, resulting in a higher dissipation of energy.

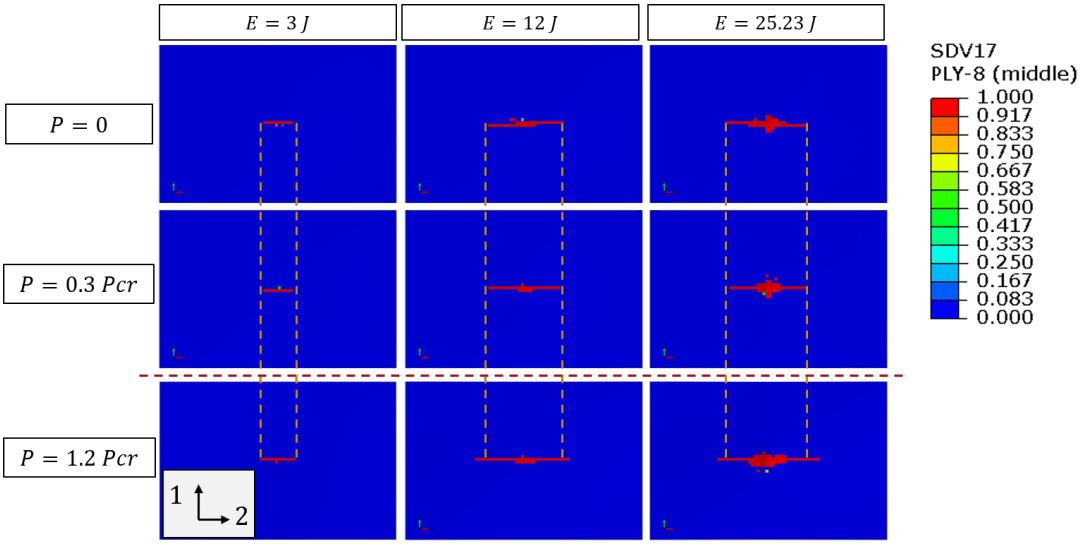

Figure 14. Damage due to compression in direction 2, top ply in contact with the impactor.

Figure 15 shows the damage due to compression along direction 2 for the fifth laminate's ply (ply above cohesive interface). Damage extension increases for higher pre-load levels by the appearance of damage near the loaded edges. At lower incident energies, where indentation is smaller and damage does not propagate near loaded edges, load cases above buckling still result in a greater damaged region.

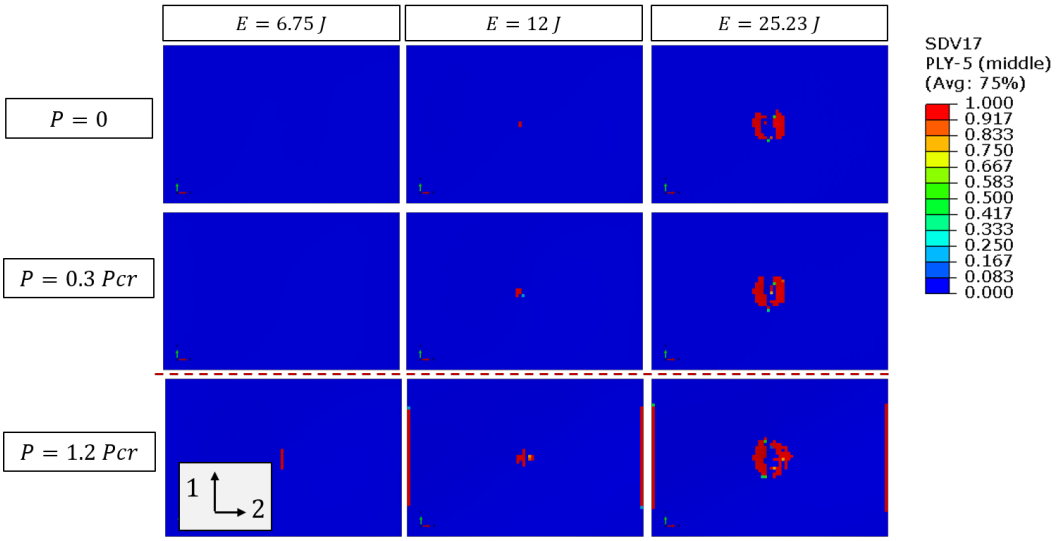

Figure 15. Damage due to compression in direction 2, ply above cohesive interface.

6. CONCLUSIONS

The use of energy based failure models implemented in ABAQUS FE code resulted in a powerful tool for parametric studies aiming to explain structure damage tolerance behaviour. The results for models with damage propagation and elastic, ABAQUS in-built, material properties showed a good correlation at low energy levels, meaning that damage propagation had little effect. As impact incident energy increases significant differences between predictions obtained using elastic and progressive damage models are observed, showing the importance of accounting for progressive failure in the impact dynamic analyses of composite structures.

The increase in the in-plane pre-load resulted in greater maximum displacement at the plate's center, representing a lower overall bending stiffness of the laminate. The delamination extension showed little dependence on the pre-stress for

the analysed cases. Total cohesive interface degraded area increases with pre-load, mainly by the appearance of damaged elements near the loaded edges. Intralaminar damage is also greater for higher pre-load levels. Consequently, the increase in intralaminar and interlaminar damaged extension resulted in the greater energy dissipation. Despite the influence of pre-load in the energy dissipation, a fairly good correlation between the predicted DTL and DTL levels predicted using the analytical expression proposed by Davies and Zhang (1995) and adapted by Olsson (2003) was found.

7. ACKNOWLEDGEMENTS

This study was financed in part by the Coordenação de Aperfeiçoamento de Pessoal de Nível Superior - Brasil (CAPES) - Finance Code 88882.180785/2018-01 and CNPq (Process No. 301053/2016-2).

8. REFERENCES

Abrate, S., 1998. *Impact on Composite Structures*. Cambridge University Press, New York, USA.

Camanho, P.P., Davila, C.G. and de Moura, M.F., 2003. "Numerical simulation of mixed-mode progressive delamination in composite materials". *Journal of Composite Materials*, Vol. 37, No. 16, pp. 1415–1438.

Davies, G. and Zhang, X., 1995. "Impact damage prediction in carbon composite structures". *International Journal of Impact Engineering*, Vol. 16, No. 1, pp. 149–170.

Hashin, Z., 1980. "Failure criteria for unidirectional fiber composites". *Journal of applied mechanics*, Vol. 47, No. 1, pp. 329–334.

Heimbs, S., Heller, S., Middendorf, P., Hähnel, F. and Weiße, J., 2009. "Low velocity impact on cfrp plates with compressive preload: Test and modelling". *International Journal of Impact Engineering*, Vol. 36, No. 10, pp. 1182 – 1193.

Olsson, R., 2003. "Closed form prediction of peak load and delamination onset under small mass impact". *Composite Structures*, Vol. 59, No. 3, pp. 341 – 349. ISSN 0263-8223.

Yokoyama, N.O., Donadon, M.V. and de Almeida, S., 2010. "A numerical study on the impact resistance of composite shells using an energy based failure model". *Composite Structures*, Vol. 93, No. 1, pp. 142–152.

Yokoyama, N.O., 2012. *Efeitos de curvatura e pressurização em cascas laminadas sujeitas a impacto*. Ph.D. thesis, Instituto Tecnológico de Aeronáutica, São José dos Campos, Brasil.

Zhang, X., Davies, G. and Hitchings, D., 1999. "Impact damage with compressive preload and post-impact compression of carbon composite plates". *International Journal of Impact Engineering*, Vol. 22, No. 5, pp. 485–509.

9. RESPONSIBILITY NOTICE

The authors are the only responsible for the printed material included in this paper.